OPEN ACCESS

University of BRISTOL

Liu, C., Heard, P., Griffiths, I., Cherns, D., & Flewitt, P. (2019). Carbide Precipitation Associated with Carburisation of 9Cr-1Mo Steel in Hot CO2 Gas. *Materialia*, [100415]. https://doi.org/10.1016/j.mtla.2019.100415

Peer reviewed version

License (if available):
CC BY-NC-ND

Link to published version (if available):
10.1016/j.mtla.2019.100415

Link to publication record in Explore Bristol Research
PDF-document

This is the author accepted manuscript (AAM). The final published version (version of record) is available online via Elsevier at https://www.sciencedirect.com/science/article/pii/S258915291930211X. Please refer to any applicable terms of use of the publisher

University of Bristol - Explore Bristol Research
General rights

This document is made available in accordance with publisher policies. Please cite only the published version using the reference above. Full terms of use are available:
http://www.bristol.ac.uk/red/research-policy/pure/user-guides/ebr-terms/

Carbide Precipitation Associated with Carburisation of 9Cr-1Mo Steel in Hot CO_2 Gas

C. Liu[1], P.J. Heard[1*], I. Griffiths[1], D. Cherns[2], P.E.J. Flewitt[1,2]

[1]Interface Analysis Centre, H.H. Wills Physics Laboratory, University of Bristol, Bristol, BS8 1TL, UK
[2]HH Wills Physics Laboratory, University of Bristol, Bristol, BS8 1TL, UK

Abstract:

Experimental ferritic 9Cr-1Mo steels exposed at high temperature and pressure to CO_2-based gas undergo oxidation and carburisation. Oxidation proceeds initially as a protective phase with parabolic kinetics (stage I). At high temperatures and longer times, more rapid "breakaway" oxidation occurs (stage II). Post-breakaway oxidation follows linear kinetics (stage III). A virgin sample and three oxidised samples were selected for analysis. Precipitates embedded in the matrix with four different morphologies were observed using focused ion beam imaging, X-ray diffraction and electron microscopy techniques. Coarse carbides ($M_{23}C_6$) were observed as the predominant precipitates in all four samples. Fine needles (M_2C), large needles (MC) and cored coarse carbide precipitates ($M_{23}C_6$) were also present in stages (I), (II) and (III), respectively. TEM analysis was used to give the lattice types and orientations of the carbides found. Energy-dispersive X-ray analysis was used to obtain compositions. The precipitation is considered particularly with respect to the formation of cored $M_{23}C_6$ carbide precipitates. These data provide a threshold for the matrix composition that defines the onset of breakaway oxidation.

Keywords: 9Cr-1Mo steel, Carburisation, Focused ion beam, X-ray Diffraction, (S)TEM-EDX

*Corresponding author: peter.heard@bristol.ac.uk

1. Introduction

The general class of 9Cr-1Mo steel has been used for tubing material and other components for many years in the Advanced Gas-cooled Reactor power stations (AGR) in the UK [1][2][3][4][5]. Changes in the mechanical and corrosion properties occur as a result of thermal ageing, oxidation and carburisation in the coolant gas containing CO_2 with traces of CO, H_2, H_2O and CH_4. The consideration of service life extension of AGRs has revived the interest in 9Cr-1Mo steel and prompted the study of the mechanisms of concurrent oxidation and carburisation [6][7][8]. The thermodynamic equilibrium reaction governing carburisation is shown by equation 1 [6][9]:

$$2CO \rightarrow CO_2 + C \downarrow \quad (1)$$

Carbon is deposited following the Boudouard reaction [10], as shown in equation 1. Some investigations proposed that carbides may be a trigger for the formation of non-protective oxide by combining with

chromium in the matrix, subsequently resulting in insufficient chromium to form the protective Cr-rich oxide scales [11][12][13].

The 9Cr-1Mo series of high alloy steels can be variously heat treated to produce either a tempered martensite or a ferrite plus carbide microstructure. When subjected to further thermal ageing this can lead to the evolution of various types of carbide and carbo-nitride precipitates [14]. Certainly, a specific carbide type that is more generally encountered is the $M_{23}C_6$ type. This has a face centred cubic crystal structure with a space group Fm-3m (No 225) with 116 atoms per unit cell, of which 92 atoms are metallic and 24 non-metallic (e.g. carbon) [15]. In general, for high alloy ferritic steels the complex crystal structure carbide precipitates contain several metallic elements, M, so that in addition to Fe it is possible that Cr, Mo, Mn etc. are present. It is recognised that the exact composition, size and distribution of these precipitates depends upon the total thermo-mechanical history and significantly influences the physical, mechanical and chemical properties of the particular 9Cr-1Mo alloy steel.

In this paper we consider the formation and type of carbide precipitates produced in the carburising CO_2 atmosphere and discuss this in the context of the evolution of these precipitates and therefore their influence on the associated oxidation process.

2. Materials and experiments

Experimental ferritic 9Cr-1Mo finned steel tube samples were prepared and subjected in autoclaves to simulated AGR coolant gas at 40 bar for different exposure temperatures and times. The chemical composition (wt.%) of the bulk steel prior to ageing is shown in Table 1. Typically, experimental virgin material of this type is prepared by normalising at 1050 ºC for 1 hr, air cooling and tempering at 760 ºC for 2 hr followed by air cooling to room temperature to produce a ferritic microstructure. A virgin sample and three oxidised samples were selected with different stages of oxidation. Exposure conditions for the four samples identified as Virgin, A, B and C are shown in Table 2.

Table 1: Chemical composition of experimental ferritic 9Cr-1Mo steel samples

Elements	C	S	Si	Mn	P	Cr	Mo	Ni	Co	Cu	Fe
Concentration (wt. %)	0.093	0.008	0.67	0.47	0.011	9.2	1.04	0.21	0.02	0.16	Balance

Table 2: Exposure conditions.

Sample	Temperature (°C)	Duration (hrs)	Weight gain ($mg \cdot cm^{-2}$)	In Breakaway?
Virgin	-	-	-	-
A	580	2542	8.9	No
B	640	1495	25.0	Yes
C	640	3883	54.3	Yes

Samples were mounted in cross-section and polished with silicon carbide paper followed by diamond paste of 1 µm size and finished with vibro-polishing using silica colloidal liquid for a few hours, depending on the surface condition of each sample. A schematic diagram of a prepared cross-section of

the finned tube sample is shown in Figure 1. A path chosen for the analysis of carbide precipitates across a fin is shown by the arrow.

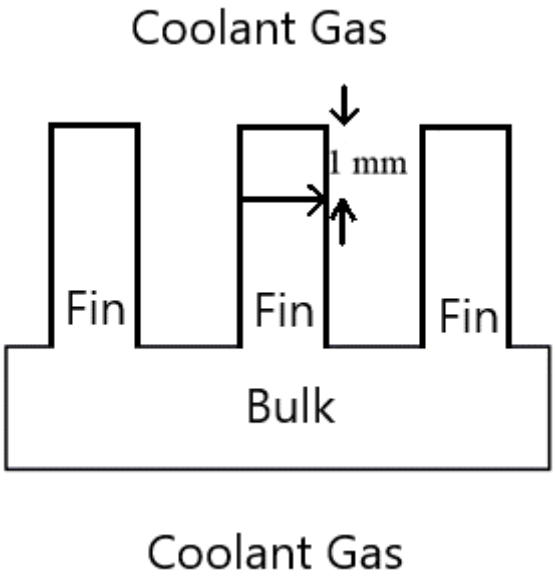

Figure 1: Schematic drawing of finned sample (not to scale), coolant gas and path for FIB/XeF_2 imaging across a fin (arrow).

An FEI FIB-201 focused gallium ion beam workstation was used for imaging the carbides. A 30 keV beam energy and 70 pA current was used for imaging. Samples were initially cleaned by sputtering an area of 120 μm × 100 μm at 11 nA beam current for about 10 s to remove surface contamination and oxide. Focused ion beam induced secondary electron images showing channelling contrast were then obtained at 70 pA beam current. XeF_2 gas was then introduced into the chamber for a few seconds to functionalise the surface and accentuate the contrast of the carbide precipitates. With the introduction of XeF_2, the resulting images have reduced ion channelling contrast but show carbide precipitates as darker regions [16].

A Philips Xpert diffractometer with a Cu Kα X-ray source was used for X-ray diffraction (XRD) analysis to identify the phases present in the samples. The generator voltage used was 40 kV and the tube emission current was 30 mA. spectra were acquired between 10° and 120° 2Θ with a step of 0.02° and 1 s dwell time. A PW3123/10 graphite monochromator was used for the Cu Kα source.

Thin foils of 15 μm × 6 μm × 0.1 μm were prepared using the gallium ion milling, lift out method in an FEI Helios NanoLab 600i combined FIB/SEM dualbeam system for subsequent transmission electron microscopy (TEM) and scanning transmission electron microscopy (STEM) analysis. A Philips EM430 instrument operating at 200 kV was used to obtain images and diffraction patterns from the phases within the thin foils. An Oxford Instruments AztecTEM equipped with an X-Max 80 EDX detector was used in the STEM mode for elemental distribution analyses.

3. Results

3.1. Carbide precipitate identification

The virgin sample and samples A, B and C were examined with XeF_2 assisted FIB imaging. The virgin sample comprised of ferrite grains of approximately 10 μm diameter with grain boundary and intragranular carbide precipitates. A focused ion beam image of sample B showing the grain structure is shown in Figure 1(a). With thermal ageing the microstructure changed so that precipitates with four different morphologies were observed, as shown in Figures 2 (b) to (e). Coarse precipitates were present at grain boundaries as well as within the grains. Additionally, intragranular fine needle precipitates (length < 700 nm) were present in the non-breakaway sample A, Figure 2(c). Cored coarse precipitates and intragranular large needle precipitates (length > 1 μm) were present in the breakaway initiation sample B, Figure 2(d), and cored coarse precipitates were observed in post-breakaway sample C, Figure 2(e). Overall in Figures 2(b) to (e) the microstructures are consistent with carbon diffusing both along grain boundaries and within grains to form intergranular and intragranular precipitates, respectively. It can be seen that the carbide precipitates in the breakaway initiation sample, Figure 2(d), possess smooth or linear boundaries, while those present in the post-breakaway sample, Figure 2(e), possess more irregular boundaries within the ferrite matrix. XRD analysis was used to identify these precipitates.

Figure 3 shows the intensity v. 2Θ trace obtained by XRD analysis of sample B as an example. In this diffraction trace both oxide and carbide precipitate peaks are identified: Fe_3O_4, $M_{23}C_6$, MC and M_2C. In addition, the peaks obtained from the ferrite matrix referred to as α-Fe are present. Table 3 shows the relative intensities of the peaks obtained from each sample, as well as the identified carbide precipitate types. The mounting material was examined separately, and the corresponding peaks noted in the spectra. The only phase detected in the virgin sample was identified as ferrite (α-Fe), which was also present in the other samples. Additionally, oxide M_3O_4 (including magnetite and spinel) was detected in sample A. However, no precipitates were detected in this sample, presumably due to their low volume fraction, see Figure 2(b). With a carbon content of 0.093 wt% in the virgin material and assuming carbide precipitates of type $M_{23}C_6$, an approximate volume fraction of 2% would be expected. The spectrum from sample B indicated the presence of MC, $M_{23}C_6$, and M_2C carbide precipitates plus α-Fe and M_3O_4. MC and $M_{23}C_6$ were also detected in sample C with α-Fe and oxide, Fe_3O_4.

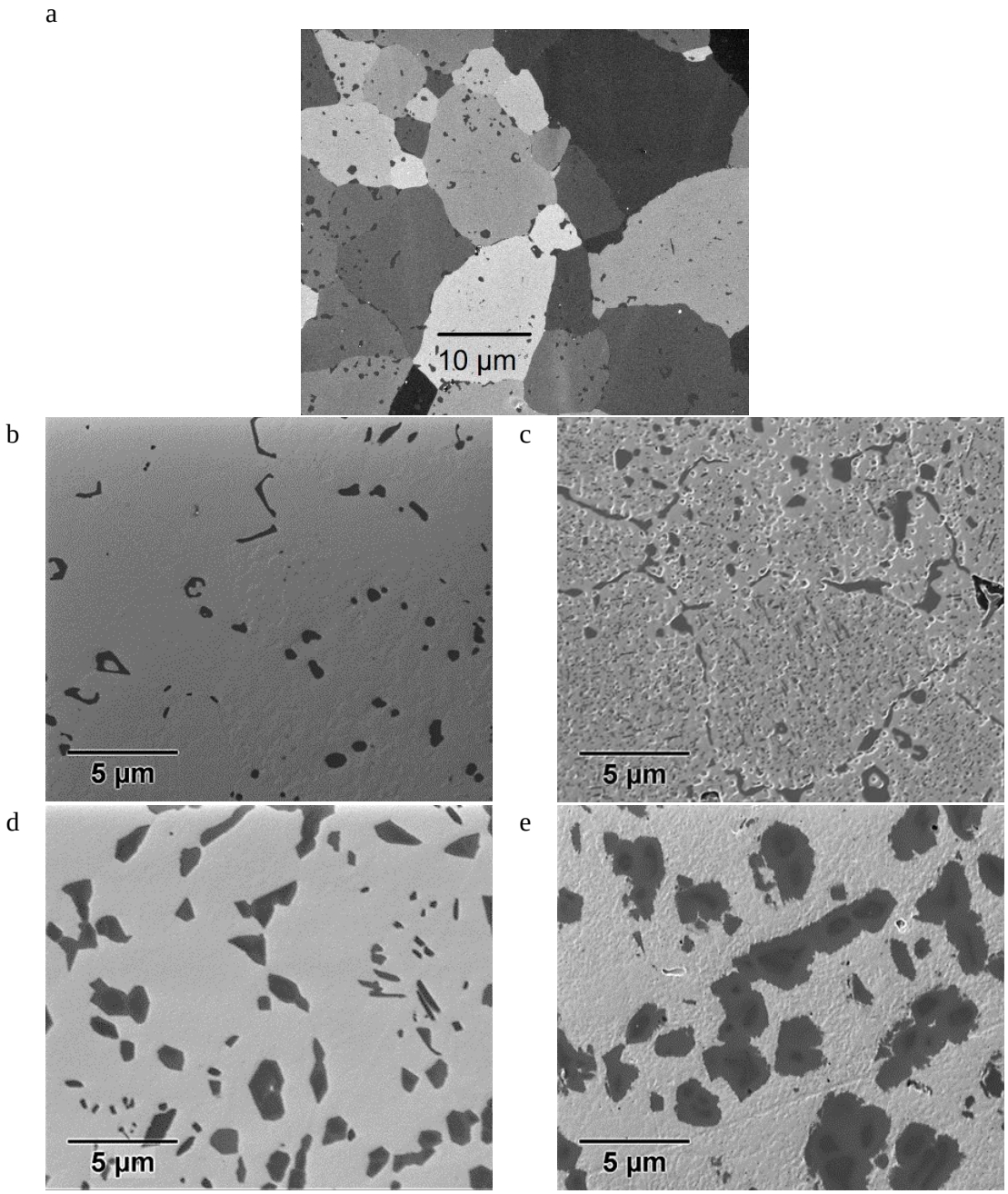

Figure 2: (a) FIB image from sample B showing grain contrast.
FIB/XeF_2 images from sample (b) Virgin; (c) sample A; (d) sample B and (e) sample C.

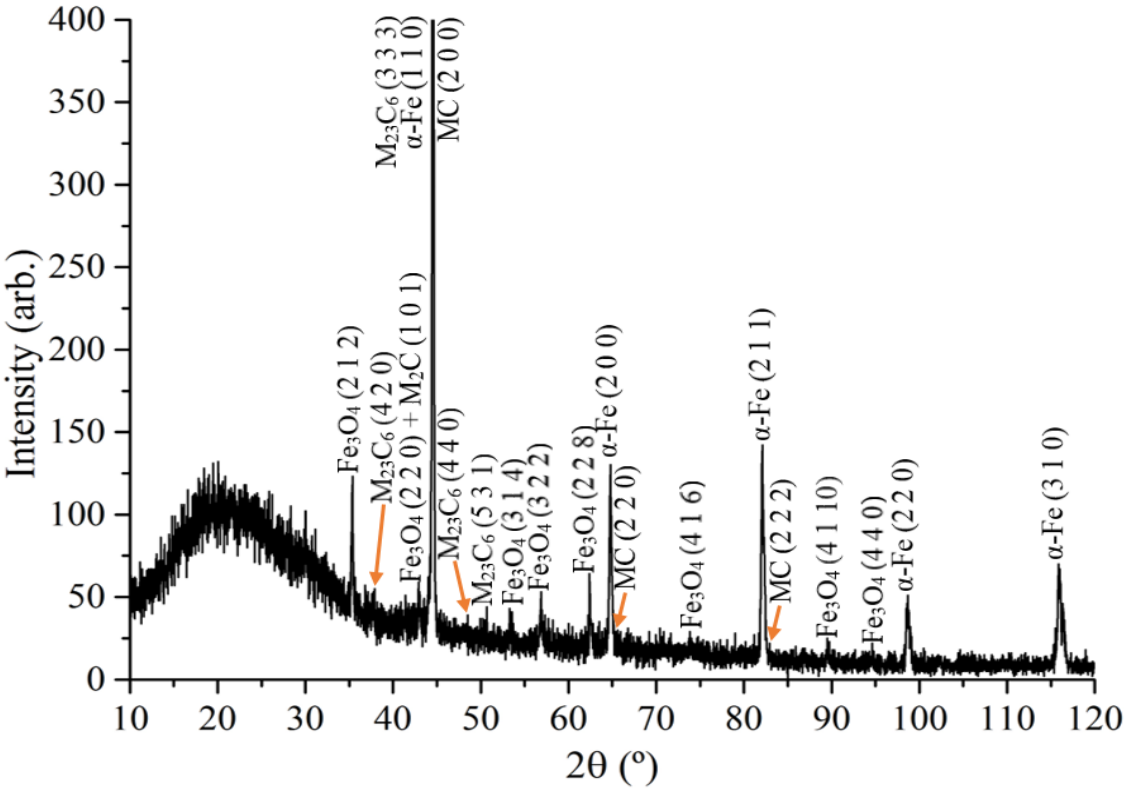

Figure 3: X-ray diffraction trace intensity v. 2Θ from sample B

Table 3. XRD data obtained from each sample.

Sample	2Θ angle（º）	Relative intensity (arb.)	Carbide type	Lattice parameter (nm)
A	44.75	917	$M_{23}C_6$	1.065
A	42.88	59	M_2C	See SAD
B	37.86	57	$M_{23}C_6$	1.061
B	44.42	768	$M_{23}C_6$	1.058
			MC	0.407
B	47.02	38	$M_{23}C_6$	1.092
B	50.69	44	$M_{23}C_6$	1.064
B	65.25	32	MC	0.404
B	82.84	23	MC	0.403
C	44.58	1077	$M_{23}C_6$	1.050
			MC	0.406
C	82.88	36	MC	0.403
C	86.69	33	Fe_3C	0.476
C	89.65	34	$M_{23}C_6$	1.070

Transmission electron microscopy was adopted to explore the precipitates with different morphologies, including coarse, fine needle, large needle and cored coarse carbides. The corresponding parent matrix was also evaluated using electron diffraction to identify the crystal structure and lattice parameters. A TEM image from sample A of a fine needle precipitate, the corresponding selected area diffraction (SAD) pattern and the equivalent from the adjacent parent matrix are shown in Figure 4(a). The fine needle precipitate had a hexagonal (HCP) structure with lattice parameters a and c of 0.25 nm and

0.42 nm, respectively. Following Andrews et al [17], the fine needle was an M_2C (where M represents Fe and Cr) with a [011] zone axis. SAD from matrix material adjacent to the carbide precipitates showed it to be α-Fe with a body-centred cubic (BCC) structure and a [011] zone axis. The mean lattice parameter was 0.29 nm, although there was a spread of values giving a standard deviation of 0.02 nm. The orientation relationship between the fine needle M_2C and the matrix was $(10\bar{1})_{M_2C}\|(01\bar{1})_{\alpha-Fe}$ and $[011]_{M_2C}\|[011]_{\alpha-Fe}$.

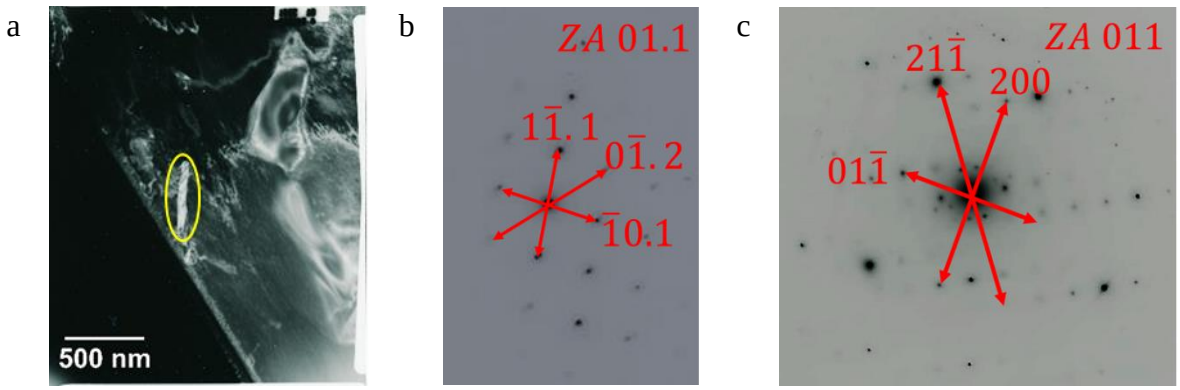

Figure 4: (a) Dark field TEM image of sample A; (b) corresponding SAD of the small needle marked (c) corresponding SAD of adjacent matrix.

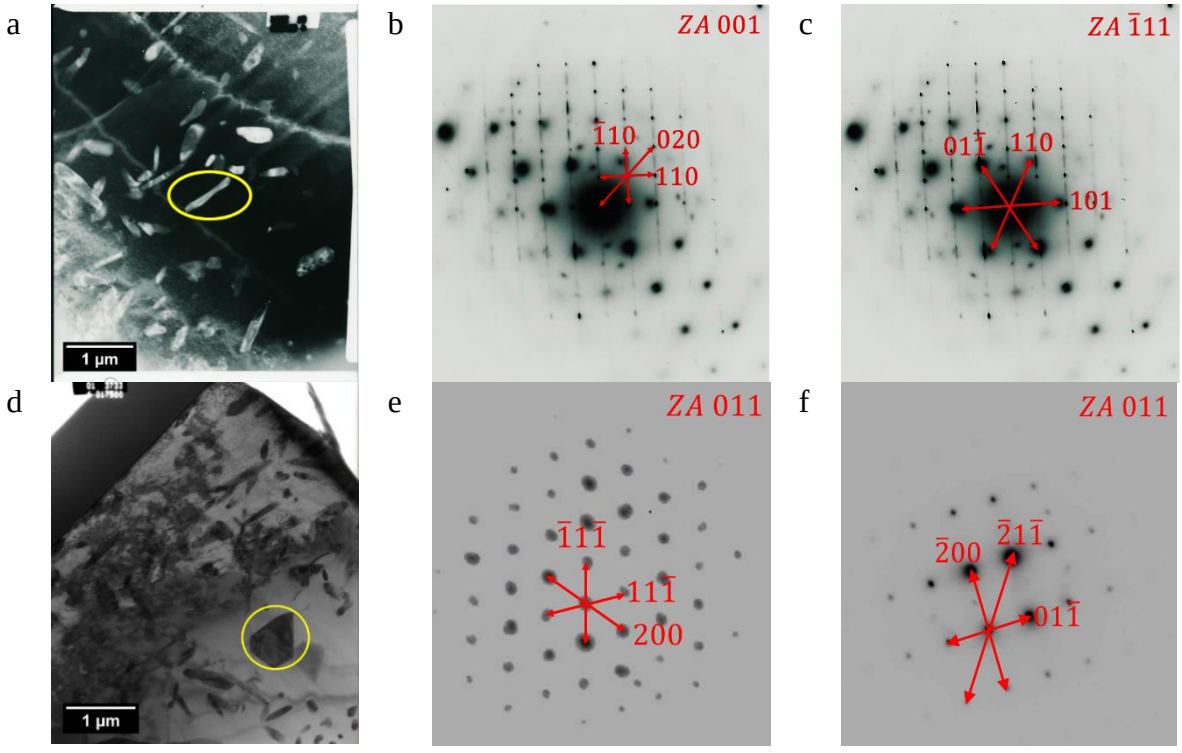

Figure 5: (a) Dark field TEM image from sample B; (b) corresponding SAD of the large needle marked; (c) SAD of adjacent matrix. (d) bright field TEM image from another grain including a coarse carbide; (e) corresponding SAD of the coarse carbide marked; (f) SAD of adjacent matrix.

TEM images and SAD patterns from a large needle and adjacent matrix for sample B are shown in Figures 5(a), (b) and (c). The large needle, about 1 µm long, was identified as MC, with a body-centred cubic (BCC) structure with a [001] zone axis, while the adjacent metal was α-Fe with a $[\bar{1}11]$ zone axis. The lattice parameter of the needle was 0.47 nm. A coarse carbide in another grain from the same thin foil was also analysed and the TEM image, SAD of the carbide and the adjacent metal are shown in Figures 5(d), (e) and (f) respectively. The coarse carbide was identified as $M_{23}C_6$ with lattice parameter 1.02 nm, with a face-centred cubic (FCC) structure in the [011] zone axis, while the adjacent metal was α-Fe in the [011] zone axis [17]. The orientation relationship between the large needle MC and the matrix was $(110)_{MC}\|(101)_{\alpha-Fe}$ and $[001]_{MC}\|[\bar{1}11]_{\alpha-Fe}$, while the relationship between the coarse carbide $M_{23}C_6$ and the matrix was $(11\bar{1})_{M_{23}C_6}\|(21\bar{1})_{\alpha-Fe}$ and $[011]_{M_{23}C_6}\|[011]_{\alpha-Fe}$.

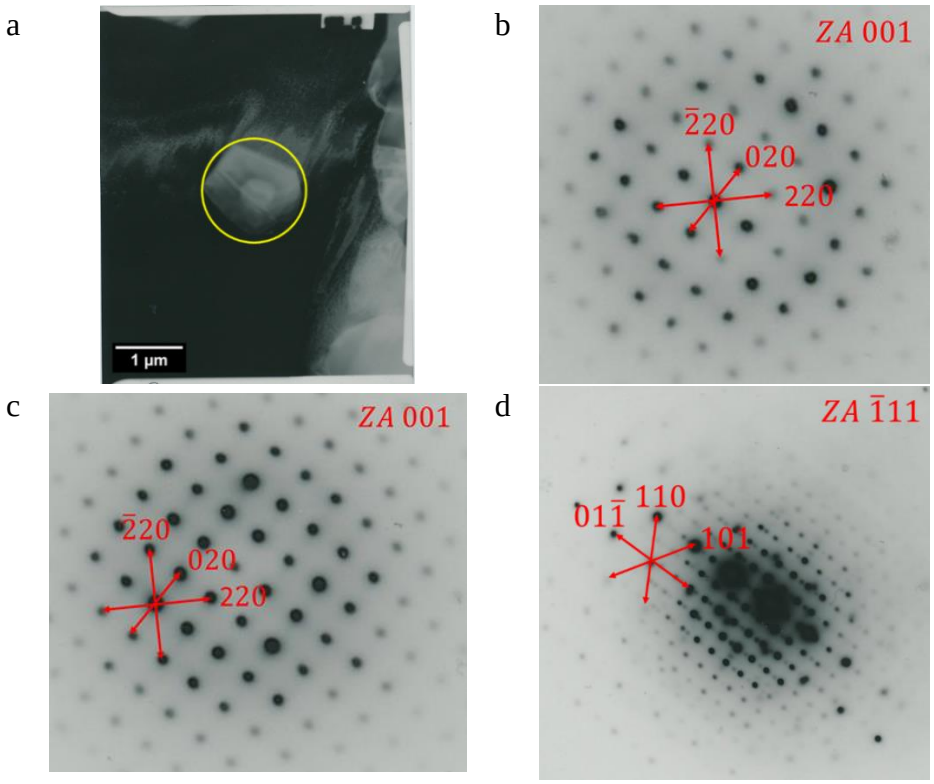

Figure 6: (a) TEM image from sample C; (b) corresponding SAD of the inner core from cored coarse carbide marked; (c) corresponding SAD of the shell from cored coarse carbide and (d) SAD of adjacent matrix.

Figure 6(a) shows a dark field image of a cored coarse carbide precipitate in sample C. SAD patterns of inner core and outer shell were evaluated, together with the adjacent matrix. These show that the core and the shell had grown in the same orientation with the [011] zone axis. However, there was a small difference in lattice parameter between the two with the former being 0.99 nm and the latter 1.01 nm. Though the atomic radius of Cr (0.130 nm) [18] is larger than Fe (0.126 nm) [19] in crystal, both Fe2+ (0.076 nm) and Fe3+ (0.064 nm) have a larger ionic radius than Cr3+ (0.062 nm) [20]. Therefore, the difference in lattice parameter between the inner core and surrounding carbide is likely to be a result of

a difference in Fe/Cr ratio between core and shell. Diffraction patterns of the adjacent parent metal identified it as α-Fe in the $[\bar{1}11]$ zone axis. The orientation relationship between the cored coarse carbide $M_{23}C_6$ and the matrix was $(200)_{M_{23}C_6} \| (0\bar{1}1)_{\alpha-Fe}$ and $[001]_{M_{23}C_6} \| [\bar{1}11]_{\alpha-Fe}$.

Since carbides with different morphologies were evaluated with TEM, their elemental distributions were obtained using STEM-EDS analysis.

3.2. Carbide composition

The thin foils were analysed in STEM mode using an Oxford Instruments AztecTEM EDS system with X-Max 80 detector. Compositions were obtained and STEM-EDS Kα1 line scans and maps of the elements of interest were acquired. As shown in the FIB images of Figure 2, only coarse carbides were present both at grain boundaries and within the grains in the virgin sample. A thin foil sample was examined using STEM-EDS as shown in Figures 7(a) and (b). The Cr concentration of intergranular carbide was approximately 80 wt.% with a very low Fe content, Figure 7(a), while the Cr and Fe concentration of the intragranular carbide was approximately 50 wt.% and 30 wt.%, respectively, Figure 7(b). As expected, the chromium concentration in the surrounding matrix was approximately 9 wt.%.

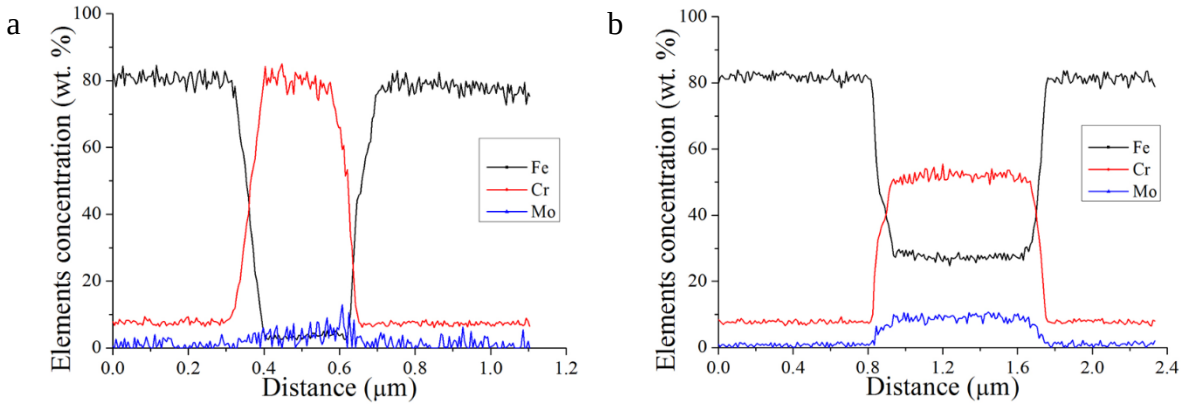

Figure 7: EDS line scan profiles across coarse carbides in the virgin sample (a) intergranular carbide; (b) intragranular carbide.

Images obtained by FIB/XeF_2 presented in Figure 2 show that coarse carbides and fine needles were present in the region close to the oxide in sample A. Coarse carbides were present both at grain boundaries and within the grains while fine needles were distributed within the grains. STEM line scan analysis of these two types of carbides is shown in Figures 8(a) and (b). A cross-section perpendicular to the c axis of a fine needle was selected to minimise any contribution from the matrix, Figure 8(a). The concentration profiles show that the fine needle is mainly comprised of Cr (50-90 wt.%) and Fe (less than 5 wt.%), Figure 8(b), whereas the Cr and Fe concentrations in the coarse carbide are approximately 50 and 30 wt.%, respectively.

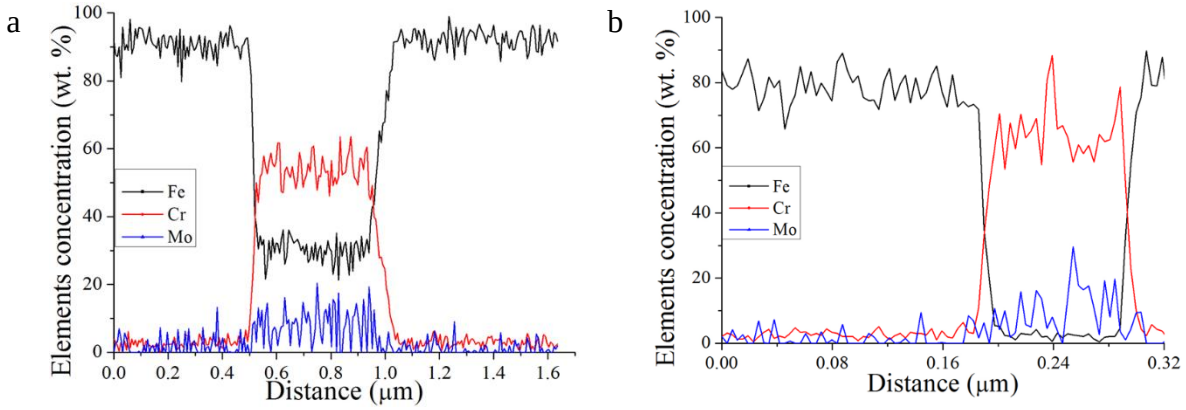

Figure 8: EDS line scan profiles across carbides in Sample A. (a) coarse carbide (b) needle carbide.

Core regions were present in some of the coarse carbides formed in the sample B which had entered breakaway initiation. The concentration profiles from a cored coarse carbide and a large needle are shown in Figure 9. These show that the Cr concentration in the core of the coarse carbide is as high as 80 wt. % but reduced to about 50 wt. % in the outer shell. The profiles also indicate that Cr is depleted in the surrounding matrix (less than 5 wt. %). The concentration profiles of the large intragranular needles, Figure 9(b) show that Cr and Fe concentrations are 40-60 wt. % and 20-40 wt. %, respectively.

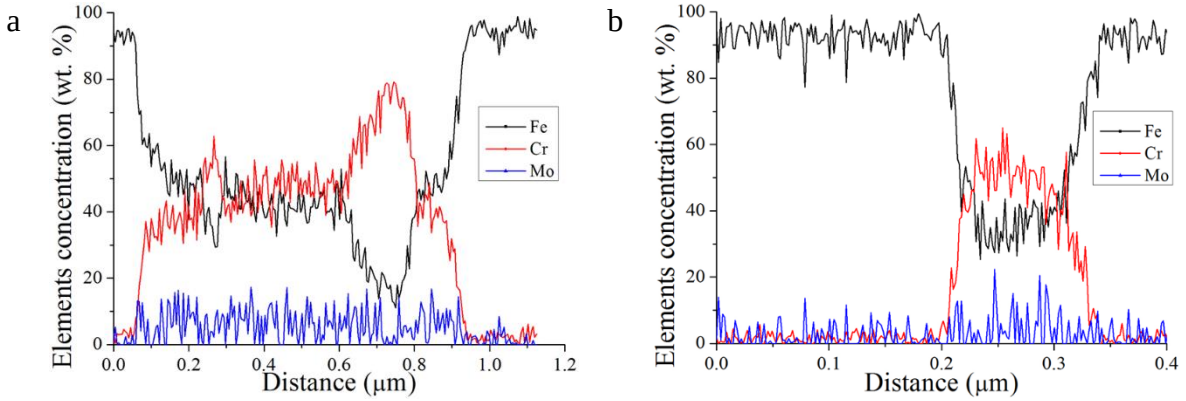

Figure 9: EDS line scan profiles across carbides in Sample B. (a) a cored coarse carbide; (b) an intragranular needle carbide.

Figures 10(a) and (b) show a STEM image and corresponding EDX profile of a cored coarse carbide precipitate from sample C. The core of the precipitate is delineated by lines on the image and the EDX profile. Both Cr and Fe concentrations in the core are around 40 wt.% (shown at 2.5 μm distance), Figure 10(b). In addition, there is significant Cr depletion in the surrounding parent matrix to around 1 wt.%. The Fe concentration is higher than the Cr concentration in the outer shell of the precipitate but for the inner core the Fe concentration is roughly equal to that of Cr. The adjacent carbide precipitate (shown at 0.8 to 1.8 μm distance) has a similar composition to the shell of the cored precipitate, and it is a possibility that this is carbide precipitate that no longer has a core, but it is more likely to be a sectioning effect such that the core lies out of the plane of the TEM section.

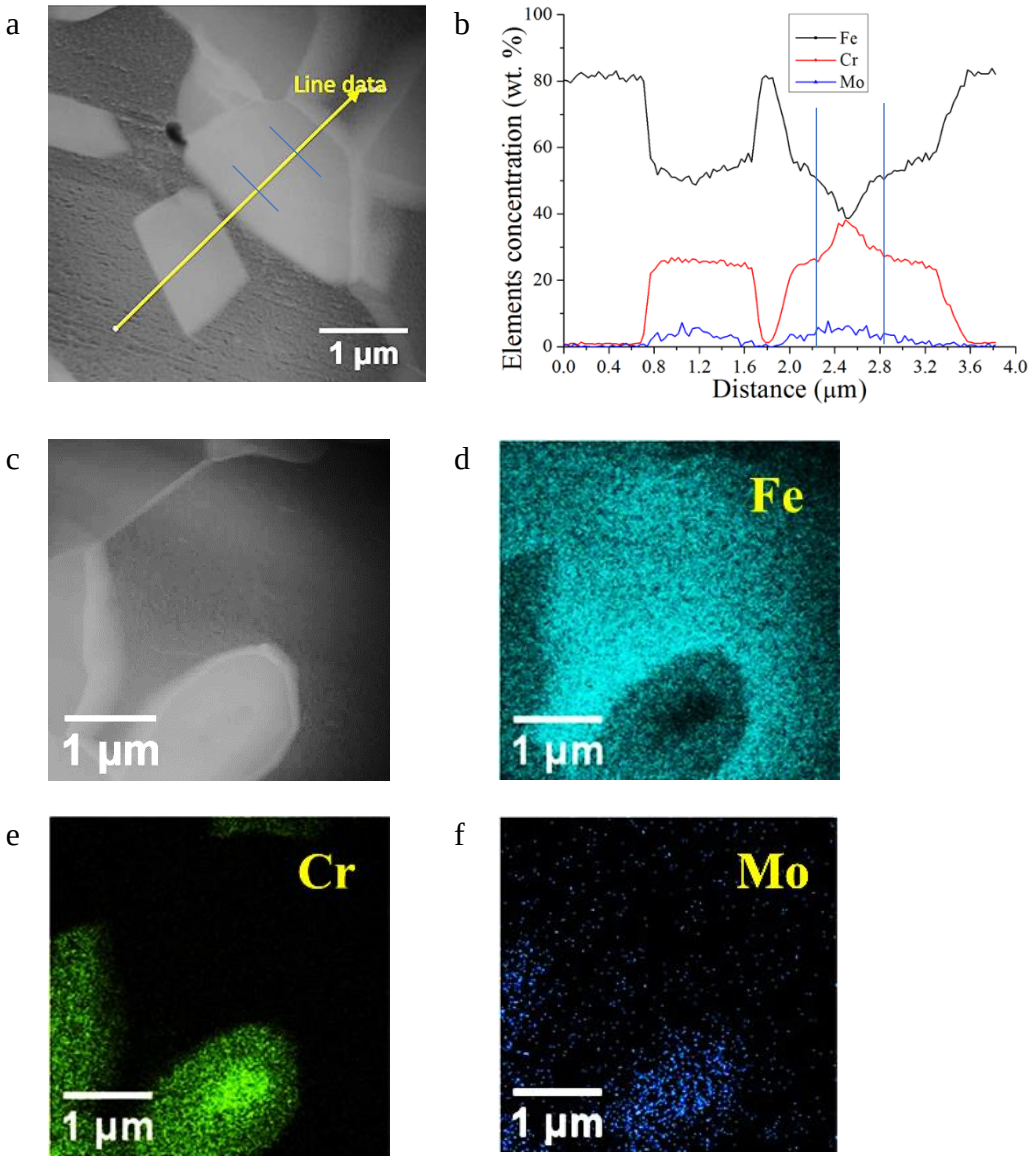

Figure 10: Sample C. (a) STEM image of an intragranular cored coarse carbide; (b) EDS line scan profile from the line in (a). (c) STEM image of intragranular cored coarse carbide with EDS maps of (d) Fe; (e) Cr and (f) Mo.

A STEM image and EDS elemental maps of a cored coarse carbide precipitate are shown in Figures 10 (c), (d), (e) and (f). As seen in Figure 2, needle carbide precipitates were absent in the virgin sample and post-breakaway sample C. The FIB images in Figure 2 show that fine needles were present after exposure at a lower temperature (580 °C) in the non-breakaway sample A. These dissolved into the matrix with increase of temperature and time. Large needles were formed in the sample which had entered breakaway initiation at higher temperature (640 °C). Both fine and large needle carbide precipitates dissolved into the metal for the formation of $M_{23}C_6$ in the post-breakaway sample C. In addition, cored coarse carbide precipitates were formed as the Cr in the matrix was depleted.

3.3. Carbide area fraction

The carbide types, morphologies and elemental distributions were identified using XRD, TEM and STEM-EDS techniques. However, it is also important to understand the distribution of carbides in the matrix, expressed as carbide area fraction as a function of position within the component. Profiles of carbide area fractions were determined using FIB/XeF_2 images such as those shown in Figure 2(b), (c), (d) and (e). The central fin of each sample was analysed by FIB/XeF_2 imaging following a horizontal path at 1 mm from the fin tip as shown in Figure 1. Five images were obtained along each line and carbide area fractions were obtained using standard image processing software (ImageJ) to threshold the images according to greyscale and count pixels.

The carbide area fraction profiles taken from the line scans at 1 mm from the fin tip for the four samples are shown in Figures 11(a) to (d). Needle carbide precipitates were distinguished from coarse carbide precipitates for samples A and B by using standard imaging software to separate them according to area. As observed from Figure 2, sample A contained fine needles and coarse carbides while sample B contained large needles and coarse carbides. The needle carbides and coarse carbides in these two samples were separated and plotted as a function of distance to the oxide/metal interface, together with the total carbide area fraction. The profiles show that there was a higher area fraction of fine needles close to the oxide/metal interface in sample A, but this reduced quickly to a very low level close to the fin centre (zero in some regions). Therefore, the carbide precipitates in this sample were predominantly coarse ($M_{23}C_6$).

The carbide area fraction profiles for samples B and C were relatively flat. The total carbide area fraction for sample B was relatively constant across the fin, between 15 % and 20 %. The levels of large needles and coarse carbide precipitates remained stable across the fin. The area fraction of coarse carbide precipitates for the post-breakaway sample (C) was also fairly constant across the fin, but at a higher level of about 30 %.

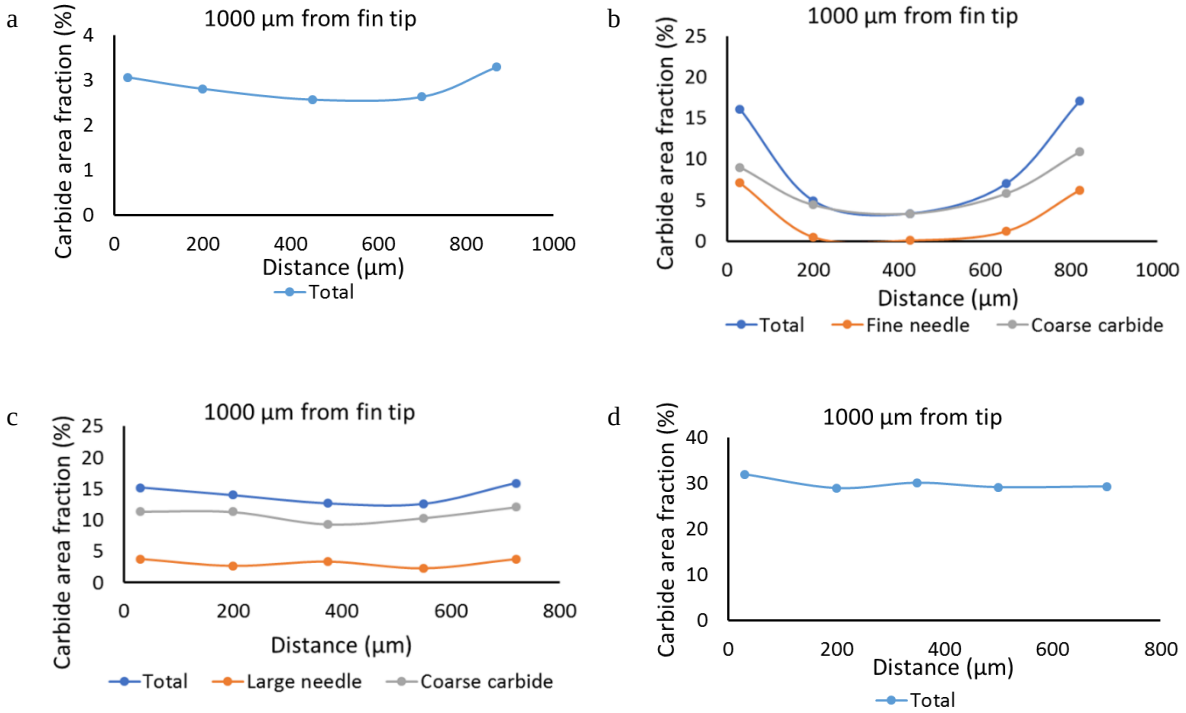

Figure 11: Carbide area fractions across the fins 1 mm from the fin tip: a) Virgin sample. b) Sample A; c) Sample B; d) Sample C.

4. Discussion

The present results show the importance of the non-equilibrium conditions, in particular associated with carbon diffusion into the steel, on the subsequent carbide precipitation. This excess carbon arises from the Boudouard reaction given in equation 1 and is therefore free to diffuse and interact to give additional carbide precipitation. During carburisation, Cr, Fe and Mo in the ferritic matrix combine with carbon to form carbide precipitates. A schematic of the proposed mechanism is shown in Figure 12. Carbides identified in the examined samples are shown Table 4. The concentrations of the key elements within the carbides and the surrounding matrix are shown in Table 5.

In the virgin material, there are pre-existing precipitates of the form $M_{23}C_6$, Figure 12(a), but as carburisation proceeds, further $M_{23}C_6$ type carbide precipitates form as well as some needle-shaped MC and M_2C precipitates. Since the MC and M_2C carbide precipitates have a high chromium content, as carburisation continues and more free carbon is released, to the point of breakaway initiation, these needle-shaped precipitates tend to go into solution as the matrix chromium concentration decreases. The predominant species then becomes $M_{23}C_6$ with a chromium content of about 50 wt.%. It has to be recognised that these $M_{23}C_6$ carbide precipitates have a complex face centred cubic crystal structure comprising typically of 116 atoms per unit cell with a space group of Fm-3m [21]. Their distribution across the fin of the tube component is consistent with the diffusion of excess carbon into the material from the outer surfaces, Figure 12(b). The precipitates form readily along grain boundaries, where carbon will be available because of its rapid diffusion, but also within the grains of the ferritic matrix.

Initially the carbide precipitates have a chromium content of about 50 wt.%, so that the chromium within the adjacent matrix becomes depleted as they form. Assuming that all the carbide precipitates are of the form $M_{23}C_6$, and that all the carbon within the material is present as carbide, a volume percentage of 19 % carbide would be expected to deplete the matrix of chromium completely. It is recognised that there will be a small contribution from Mo for these precipitates. Observations of the carbide precipitate profiles across the fins indeed show a flat profile of this magnitude at the breakaway initiation condition, Figure 12(c). The matrix material now becomes sensitised to accelerated oxidation.

Table 4: Carbides present in each sample.

Sample	*Small needles (M_2C)*	*Large needles (MC)*	*Coarse carbides ($M_{23}C_6$)*	*Cored coarse carbides ($M_{23}C_6$)*
Virgin			✓	
A	✓		✓	
B		✓	✓	✓
C			✓	✓

Table 5: Concentrations of Cr and Fe in the carbide precipitates and Cr concentration in the surrounding matrix (wt.%).

Element and position	*Small needles (M_2C)*	*Large needles (MC)*	*Coarse carbides ($M_{23}C_6$)*	*Cored coarse carbides ($M_{23}C_6$)*	
				Core	*Shell*
Cr in carbide	*50-90*	*40-60*	*50*	*40-80*	*30-50*
Fe in carbide	*<5*	*20-40*	*30*	*15-40*	*50-55*
Cr in surrounding matrix	*~5*	*~2*	*1 (post-breakaway)-9 (virgin)*	*~1*	

With the matrix now depleted of chromium, further carbon entering the material forms additional carbide precipitate, first by initiating with existing carbide precipitates, initially forming a shell of lower-chromium $M_{23}C_6$ carbide (Cr about 28 wt.%). It is proposed that chromium diffuses outwards from the carbide precipitate to form a low-chromium $M_{23}C_6$ outer shell, while carbon diffuses inwards, so that as further carburisation progresses, the high-chromium core becomes smaller, and the outer shell becomes larger, Figure 12(d). Observations of the cored carbide precipitates, Figure 2(e), reveal an irregular outer boundary to the carbide, consistent with a low boundary energy condition, while the interfaces between the core and shell remain relatively straight and sharp. Assuming $M_{23}C_6$ carbide precipitates of 28 wt.% chromium existed within the material, a volume percentage of about 30% would be consistent with a matrix depleted of chromium, and this is indeed the level at which the carbide coverage reaches in the post-breakaway stage.

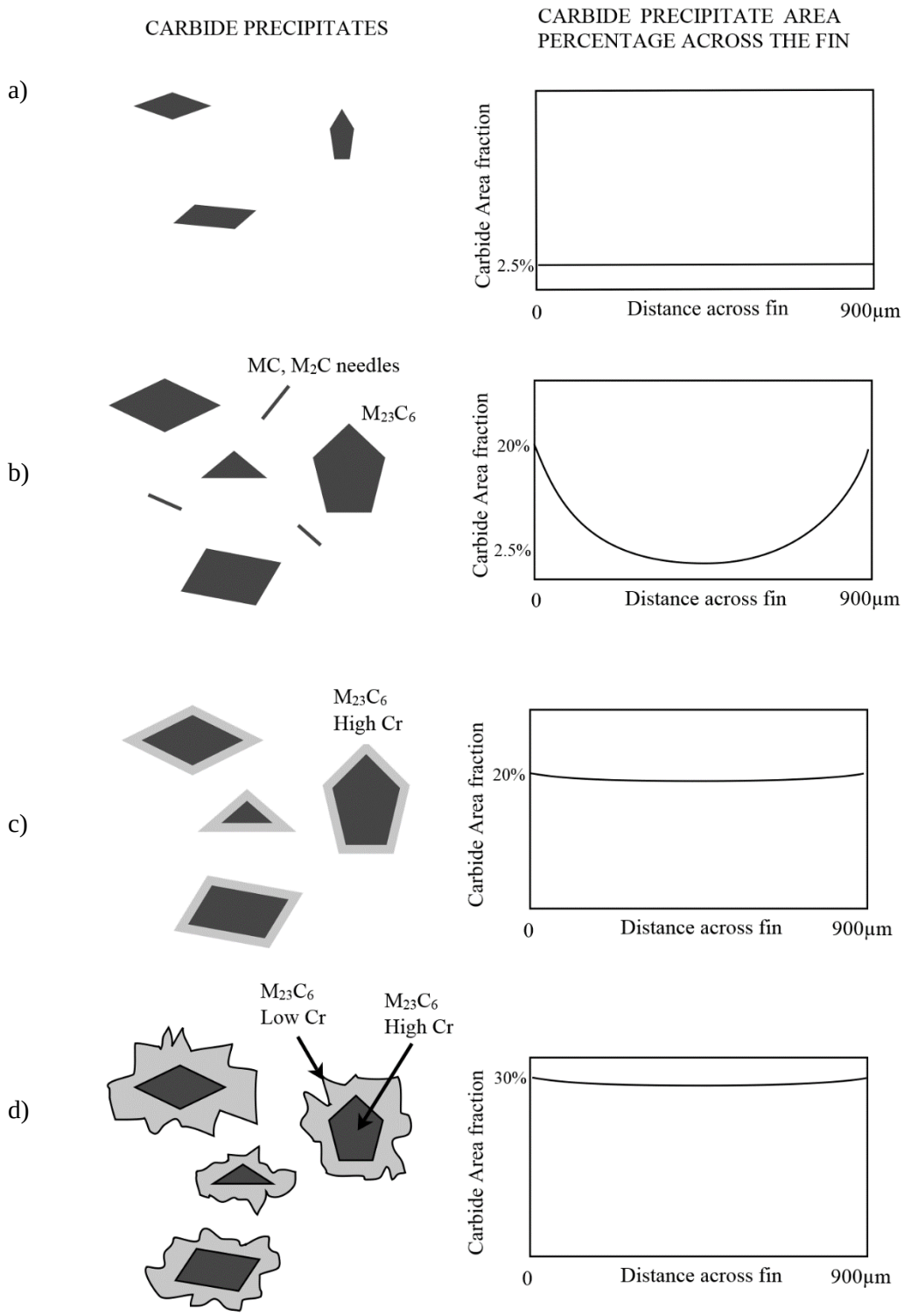

Figure 12. Schematic representation of carburisation. a) Virgin material. b) Pre-breakaway condition with high-Cr content $M_{23}C_6$ carbide precipitates. c) Breakaway initiation condition with high-Cr content $M_{23}C_6$ carbide precipitates and low matrix Cr content. d) Post-breakaway condition with cored $M_{23}C_6$ carbide precipitates containing high-Cr cores and low-Cr shells.

If carburisation were allowed to continue, presumably the precipitate cores would be consumed entirely, leaving only low-chromium carbide, but the rapid concurrent oxidation prevents this observation before the fin becomes completely oxidised. The flat profile of the precipitate area percentage across the fin is consistent with the rapid diffusion rate of carbon within the material, compared with the diffusion of chromium and carbon within the carbides, which is assumed to be much slower.

From the preceding summary of the complex precipitation of $M_{23}C_6$ carbide it is clear that the non-equilibrium conditions associated with the oxidation and carburisation processes in the 9Cr-1Mo steel heat treated to have a ferrite matrix is significant. The carburisation sequence postulated in Figure 12 provides a basis for evaluating the change in the chromium (and molybdenum) concentrations within the ferrite matrix, which will modify the oxidation characteristics. This will form the basis of a further paper addressing the important in-service consideration of the transition from exponential to linear breakaway oxidation kinetics.

5. Conclusions

During exposure of 9Cr-1Mo finned steel tubes to hot CO_2 gas, carburisation and oxidation occur concurrently. Initially coarse carbide precipitates of the form $M_{23}C_6$, and needle-shaped precipitates of the form MC and M_2C were observed in the bulk of the material. As carburisation progressed however, the needles decreased in density and the coarse carbide precipitates of form $M_{23}C_6$ dominated. A simple model is presented, in which carbon diffuses rapidly into the material, forming such carbide precipitates and depleting the remaining ferritic matrix of chromium. A flat profile of carbide volume percentage across a fin of the material is consistent with the formation of high-chromium $M_{23}C_6$ carbide precipitates (Cr content about 50 wt.%) that deplete the matrix of chromium. Further carburisation proceeds by transformation of the high-chromium precipitates to those with a lower chromium concentration by outward diffusion of chromium and inward diffusion of carbon, so that the volume percentage of precipitate in the sample fin is allowed to rise to about 30 %. The depletion of chromium in the matrix leaves the material in a state that is sensitive to oxidation, and the fin becomes rapidly consumed.

6. Acknowledgements

Financial support from the China Scholarship Council and EDF Energy is gratefully acknowledged. This paper is published by permission of EDF Energy. The views expressed are those of the authors and not necessarily EDF energy.

References

[1] G.R. Odette, On the Status and Prospects for Nanostructured Ferritic Alloys for Nuclear Fission and Fusion Application with Emphasis on the Underlying Science, Scr. Mater. 143 (2018) 142–148.

[2] H. Zhu, Comparison of Interfacial Strengthening in Creep Deformation and Radiation Damage Processes of Advanced Structural Materials for Nuclear Applications, JOM. 70 (2018) 219–228.

[3] M.N.H. Comsan, Status of Nuclear Power Reactor Development, in: 6th Conf. Nucl. Part. Phys., Luxor, Egypt, 2007: pp. 79–89.

[4] M.G. Angell, S.. Lister and A. Rudge, The Effect of Steam Pressure on the Oxidation Behaviour of Annealed 9Cr-1Mo Boiler Tubing Material, in: 15th Int. Conf. Prop. Water Steam, Berlin, 2008: pp. 1–9.

[5] E. Nonbel, Description of the Advanced Gas Cooled Type of Reactor (AGR), Rise National Laboratory Roskilde, Denmark, 1996.

[6] F. Rouillard, G. Moine, M. Tabarant and J.C. Ruiz, Corrosion of 9Cr Steel in CO_2 at Intermediate Temperature II: Mechanism of Carburization, Oxid. Met. 77 (2012) 57–70.

[7] C. Liu, P.J. Heard, S.J. Greenwell and P.E.J. Flewitt, A study of breakaway oxidation of 9Cr–1Mo steel in a Hot CO2 atmosphere using Raman spectroscopy, Mat. High Temp. 35:1-3 (2017) pp 50-55

[8] C. Liu, P.J. Heard, O.D. Payton, L. Picco and P.E.J. Flewitt, A comparison of two high spatial resolution imaging techniques for determining carbide precipitate type and size in ferritic 9Cr-1Mo steel, Ultramicroscopy 205 (2019) pp 13-19

[9] F. Rouillard and T. Furukawa, Corrosion of 9-12Cr Ferritic–Martensitic Steels in High-Temperature CO_2, Corros. Sci. 105 (2016) 120–132.

[10] J. Hunt, A. Ferrari, A. Lita, M. Crosswhite, B. Ashley and A.E. Stiegman, Microwave-specific Enhancement of the Carbon–carbon Dioxide (Boudouard) Reaction, J. Phys. Chem. C. 117 (2013) 26871–26880.

[11] C.S. Giggins and F.S. Pettit, Corrosion of Metals and Alloys in Mixed Gas Environments at Elevated Temperatures, Oxid. Met. 14 (1980) 363–413.

[12] G.H. Meier, W.C. Coons and R.A. Perkins, Corrosion of Iron-, Nickel-, and Cobalt-base Alloys in Atmospheres Containing Carbon and Oxygen, Kluwer Academic Publishers-Plenum Publishers, 1982.

[13] T. Gheno, D. Monceau and D.J. Young, Mechanism of Breakaway Oxidation of Fe–Cr and Fe–Cr–Ni Alloys in Dry and Wet Carbon Dioxide, Corros. Sci. 64 (2012) 222–233.

[14] H.K.D.H. Bhadeshia and R.W.K. Honeycombe, Steels: microstructure and properties, 2006, 3rd edition, Elsevier (London) pp 264-267

[15] Y Lim, Y Jiang, J Xing, R Zhou and J Feng, Mechanical Properties and Electronic Structures of $M_{23}C_6$ (M=Fe, Cr, Mn) type multicomponent carbides, J Alloys and Compounds (2015), 648, 874-880

[16] C. Liu, P.J. Heard, O.D. Payton, L. Picco and P.E.J. Flewitt, A Comparison of Two High Spatial

Resolution Imaging Techniques for Determining Carbide Precipitate Type and Size in Ferritic 9Cr-1Mo Steel, Ultramicroscopy, to be published.

[17] K.W. Andrews, D.J. Dyson and S.R. Keown, Interpretation of Electron Diffraction Patterns, 2nd ed., Springer US, Boston, MA, 1967.

[18] M. Okada, T. Chou, A. Kamegawa, T. Tamura, H. Takamura, A. Matsukawa and S. Yamashita, Ti–Cr–X Protium Absorbing Alloys with High Protium Content for Fuel-cell, J Alloy Comp 356-357 (2003) 480-485.

[19] F.Z. Cui, Y.D. Fan, Y. Wang, A.M. Vredenberg, H.J.G. Draaisma and R. Xu, A New Magnetic Multilayer System: Iron-bismuth. J Appl Phys, 68 (1990) 701-704.

[20] J.M. Baker, J. Kuriata, A.C. O'Connell and L. Sadlowskis, Studies of Chromium-doped Sodium Ammonium Sulphate Dihydrate: I. Electron Paramagnetic Resonance of Cr^{3+}, J Phys Condens Mat, 7 (1999) 2321-2331.

[21] Z.Q. Lv, F. Dong, Z.A. Zhou, G.F. Jin, S.H. Sun and W.T. Fu, Structural Properties, Phase Stability and Theoretical Hardness of $Cr_{23-x}M_xC_6$(M=Mo,W; x=0-3), J Alloy Comp 607 (2014) 207-214.